Fuel 403 (2026) 136130

Contents lists available at ScienceDirect

Fuel

journal homepage: www.elsevier.com/locate/fuel

Full Length Article

Adsorptıon kinetics and mechanism of hydrogen on pristine and functionalized multi-walled carbon nanotubes

Zeynep Bicil

Balikesir University, Faculty of Science and Literature, Department of Chemistry, 10145 Çağış, Balıkesir, Turkey

ARTICLE INFO

Keywords:
MWCNT
Functionalization
Hydrogen storage
Kinetics
Mechanism

ABSTRACT

This study explores the impact of hydroxyl (–OH) and carboxyl (–COOH) functionalization on the hydrogen adsorption behavior and mechanisms of multi-walled carbon nanotubes (MWCNTs). MWCNT-OH and MWCNT-COOH samples were synthesized via oxidation reactions and characterized using BET, FTIR, Raman, TG, TEM, SEM/EDX, and AFM techniques. Functionalization reduced the BET surface area but notably increased mesopore volume. FTIR spectra confirmed the presence of hydroxyl and carbonyl groups at 3432 cm^{-1} and 1755 cm^{-1}, respectively. Raman analysis showed shifts in the D, G, and 2D bands, while EDX results indicated a decrease in carbon content and an increase in oxygen content after functionalization. Thermal analysis revealed that the degradation profiles of the samples were altered. TEM and SEM images illustrated improved dispersion and separation of nanotubes upon functionalization. AFM analysis indicated significant changes in surface roughness and topography, suggesting modifications in nanotube structure. Hydrogen storage capacity was measured at cryogenic temperatures under varying pressures and time intervals. MWCNT-OH demonstrated the highest storage capacity (1.023 wt% at 80 bar). Storage rates increased with pressure, and kinetic data were best fitted to the pseudo-second-order model, with equilibrium achieved in approximately 2 min, supporting a physisorption mechanism. Mechanistic evaluation using Boyd, Avrami, and Weber–Morris models revealed a two-step adsorption process: initial adsorption on the external surface followed by diffusion into mesopores. The consistency between experimental and calculated q_e values further validated the pseudo-second-order model. The q_t vs $t^{1/2}$ plots produced two intersecting lines, confirming the two-stage adsorption behavior described by the Weber–Morris model. These findings highlight the potential of oxygen-functionalized MWCNTs as efficient, metal-free materials for advanced hydrogen storage applications.

1. Introduction

Global energy demand is steadily increasing with ongoing urbanization and industrialization [1,2]. Fossil fuels—oil, natural gas, and coal—remain dominant but are depleting rapidly. Their use contributes significantly to environmental issues such as greenhouse gas emissions, ozone depletion, acid rain, and pollution. Although still widely used, the negative impacts of fossil fuels and rising energy costs are driving the global shift toward renewable alternatives [3]. Renewable energy sources like hydraulic, solar, wind, geothermal, biomass, and hydrogen are favored for their sustainability and minimal ecological footprint [4–6]. Their widespread adoption helps mitigate environmental problems while diversifying the global energy supply [7,8]. Among these, hydrogen is considered especially promising due to its exceptionally high energy density—three times that of gasoline—and its potential to support clean energy transitions in the 21st century [9,10]. Hydrogen is a clean-burning fuel that does not release greenhouse gases or ozone-depleting substances, and it produces minimal pollutants during combustion [11]. However, economic barriers—especially related to production, storage, and infrastructure—limit its widespread use [12].

Hydrogen can be stored through various methods, including high-pressure gas, cryogenic liquids, electrochemical process, metal hydrides, and carbon-based materials [13–15]. Each approach poses unique challenges such as safety concerns, low volumetric energy density, or high operational costs [16]. Zhang et al. (2019) studied the impact of milling time on the hydrogen storage performance of Mg–Ce–Ni–Al alloys for Ni-metal hydride batteries [18]. Heydariyan et al. (2024a) used a one-step auto-combustion method to produce $SmMn_2O_5/Mn_2O_3$ nanomaterials, achieving 6.99 wt% hydrogen capacity [19]. Monsef and Salavati-Niasari (2024) synthesized $NH_4V_4O_{10}$–SnO_2 nanocomposites with excellent capacity and cycling stability [20]. Kianpour et al. (2013) reported morphology-controlled

E-mail address: zeynepbicil@balikesir.edu.tr.

https://doi.org/10.1016/j.fuel.2025.136130
Received 7 May 2025; Received in revised form 15 June 2025; Accepted 24 June 2025
Available online 26 June 2025

$NiMoO_4$ nanorods [21]. Other related studies include Behpour et al. (2009) [22], Salavati-Niasari et al. (2010) [23], Mohandes & Salavati-Niasari (2013) [24], and Amiri et al. (2018) [25], exploring corrosion inhibition, ZnS nanotubes, $AgVO_3$ microstructures, and biologically active $NiFe_2O_4$ nanoparticles respectively. Among carbon-based storage materials, activated carbon, carbon nanotubes (CNTs), graphene, fullerenes [26], and metal organic frames (MOFs) stand out due to their low cost, lightweight nature, and tunable structures. MXenes offer superior conductivity but are prone to oxidation and require complex synthesis [27]. MOFs, although highly porous and chemically tunable, often lack thermal stability and are expensive to produce [28].

Carbon-based materials, including the MWCNTs in this study, offer a practical balance of modifiability, cost, and performance. Their fast adsorption kinetics and adaptability make them ideal for hydrogen storage despite slightly lower capacities than MOFs [28–30]. Numerous theoretical and experimental studies have examined the hydrogen storage potential of these materials. For instance, Doğan et al. (2020) [29] and Işınkaralar et al. (2022) [31] produced activated carbon from fruit peels and chestnut shells respectively, with the latter achieving 3.18 wt% capacity. Fullerene nanocages and rGO/Zr-MOF composites also showed promise, as did alkali metal-doped CNTs and mesoporous carbon from rice husk [32,33].

CNTs—first discovered by Iijima in 1991—are nanostructures known for their cylindrical geometry and are available in single- and multi-walled forms [34]. They synthesizes via arc discharge, laser ablation, and especially chemical vapor deposition (CVD) [21–25]. Their applications span electronics, energy storage, catalysis, and medicine [17]. Several studies highlight the potential of functionalized MWCNTs for improved hydrogen storage, including work by Tahermansouri et al. (2013), Azizian et al. (2011), and Çakır et al. (2021) [30,35,36]. Functionalization with Schiff bases, hydroxyl, and aryl groups has enhanced their storage capacity and surface interactions. Further studies by Çalışır et al. (2021), Yalçınkaya et al. (2024), and Çakir et al. (2025) demonstrated improved performance through microwave-assisted synthesis, lithium doping, and Schiff base modifications respectively [37–39].

Despite increasing global interest in hydrogen storage, most published studies have focused primarily on improving storage capacity through the use of metal-doped or composite carbon materials, often neglecting the underlying adsorption kinetics and mechanisms. The central hypothesis is that oxygen-containing surface functionalities enhance hydrogen storage by increasing mesoporosity and altering surface interactions. To the best of our knowledge, there are no studies investigating the hydrogen storage capacity, kinetic analysis and adsorption mechanism of functionalized MWCNTs. Therefore, the study's objectives include synthesizing hydroxyl- and carboxyl-functionalized MWCNTs, characterizing their structure, measuring pressure-dependent hydrogen storage, and analyzing adsorption kinetics and mechanisms using advanced modeling. This study introduces a novel approach using only oxygen-containing groups (–OH and –COOH) to functionalize MWCNTs without metallic or polymeric dopants. In addition to structural characterization (Brunner–Emmett–Teller (BET), Fourier transform infrared spectroscopy (FTIR), Raman analysis, thermogravimetry (TG), transmission electron microscopy (TEM), scanning electron microscopy/energy dispersive X-ray spectroscopy (SEM/EDX) and atomic force microscopy (AFM), this work applies multiple kinetic models (pseudo-second-order, Boyd, Avrami, Weber–Morris) to explore adsorption kinetics and mechanisms. This safe, cost-effective and environmentally friendly strategy also supports a sustainable energy future in alignment with the United Nations Sustainable Development Goals (SDGs), particularly Goal 7: Affordable and Clean Energy.

2. Materials and methods

2.1. Materials

Except for MWCNT, all other chemicals used in the study were in analytical grade. MWCNT was purchased from the Nanografi company.

2.2. Methods

2.2.1. Purification of MWCNT

In order to remove unwanted contaminants and by-products, MWCNT samples were subjected to purification procedure by the following method. 10 g of MWCNT and 200 mL of 5 M HCl solution was placed in a 500 mL flask and kept in an ultrasonic bath at 30 °C for 2 h. This mixture was then refluxed at 70 °C for 48 h. At the end of the reflux process, the mixture was kept in an ultrasonic bath for another hour. After these processes, 500 mL of pure water was added to the reaction flask and dilution was performed. The diluted mixture was filtered by washing with plenty of water until the pH of the filtrate reached 7 in a vacuum filtration device. The obtained MWCNT sample was kept in an oven at 60 °C for 24 h and then dried in a vacuum oven at 60 °C [38].

2.2.2. Synthesis of MWCNT-OH

1 g of MWCNT and 60 mL of 0.3 m $FeCl_2{\cdot}4H_2O$ were mixed in a flask and then subjected to ultrasonication at 30 °C for 1 h. Subsequently, the mixture was placed on a magnetic stirrer, and 240 mL of 30 % H_2O_2 was slowly added dropwise. The reaction was allowed to proceed for 12 h under continuous stirring. The resulting mixture was then filtered and washed several times with 5 % hydrochloric acid. In the final step, the product was rinsed with deionized water, and washing continued until the pH of the filtrate reached neutral (pH 7). The product was dried in a vacuum oven at 60 °C for 24 h [40]. This product was named MWCNT-OH. The reaction scheme is shown in Fig. 1

2.2.3. Synthesis of MWCNT-COOH

To add carboxyl groups to the surface of MWCNTs, an acidic process was typically applied. This process is usually carried out using a mixture of sulfuric acid (H_2SO_4) and nitric acid (HNO_3). This mixture facilitates the formation of carboxyl groups (–COOH) by adding oxygen to the carbon atoms on the surface of the nanotubes. In this study, H_2SO_4 and HNO_3 were slowly added in a 3:1 ratio to 1 g of MWCNT. The mixture was kept in an ultrasonic bath for 3 h, and at the end of sonication, the solution was diluted with distilled water and filtered. When the pH of the filtrate reached 7, the MWCNTs were considered to be acid-free and

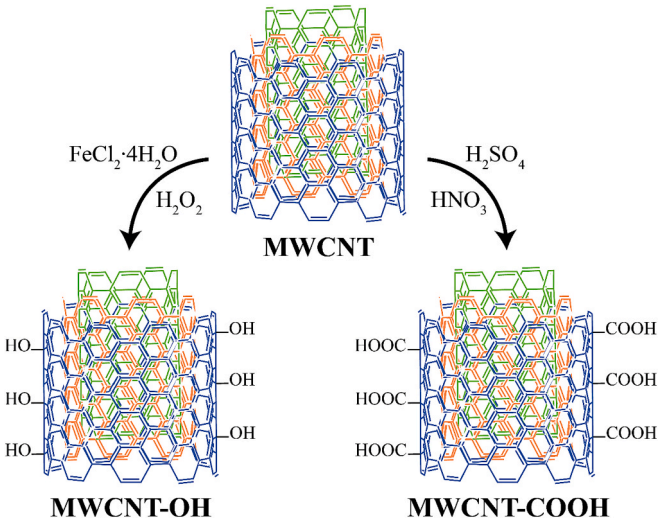

Fig. 1. The reaction schema of MWCNT-OH and MWCNT-COOH from MWCNT.

were dried in a vacuum oven overnight [41]. The obtained product was named MWCNT-COOH. The reaction for the synthesis of MWCNT-COOH from MWCNT is shown in Fig. 1.

2.3. Characterization

MWCNT and functionalized MWCNT samples were characterized using BET, FTIR, Raman, TG, TEM, SEM/EDX, and AFM techniques. Prior to BET surface area measurements and pore size analyses, the samples were degassed at 105 °C for 24 h. The surface area measurements and pore size distributions of the degassed samples were performed using pure nitrogen gas as the adsorbate in a liquid nitrogen environment (77 K) with a Quantachrome Nova 2200e series device. The BET surface areas and pore volumes of MWCNT and functionalized MWCNT samples were calculated using the NLDFT model implemented in the instrument's software. The Perkin Elmer Spectrum 100 device was used for FTIR analyses; the FTIR spectra of the samples were obtained by preparing pellets with KBr in the wavenumber range of 4000–400 cm⁻1. Raman spectra were recorded by a Renishaw Raman system with the excitation line at 532 nm. TG thermograms were obtained in the temperature range of 35–1000 °C under a nitrogen atmosphere with a heating rate of 20 °C per minute. TEM images of MWCNT and MWCNT-OH were taken using the Hitachi HT7800 system at an acceleration voltage of 100 kV. SEM images of MWCNT and functionalized MWCNT samples were obtained with the Zeiss EVO LS 10 device at a magnification of 25 KX, and EDX analyses were performed using a Bruker detector at an acceleration voltage of 20 kV. Changes in the topography of the samples were analyzed with Nanosurf Easyscan 2 AFM using a "tapping" mode probe (Tap190AL-G) at 0 mV fixed amplitude, 48 N/m field, 190 kHz frequency in air and room conditions. The surface scan was performed perpendicular to the cantilever axis at a frequency of 1 Hz with a 5x5 μm^2 experimental scanning area.

2.4. Hydrogen storage

Hydrogen adsorption measurements of MWCNT and functionalized MWCNTs were performed using Hiden IMI PSI gas storage device. The hydrogen storage capacities of the samples degassed at 105℃ for 4 h before analysis was measured at cryogenic temperature depending on the pressure [42].

3. Results and Discussion

3.1. Characterization

3.1.1. FTIR analysis

Functionalization is carried out for different purposes such as increasing the electrical conductivity of CNTs, preventing agglomeration, improving metal removal, and increasing energy storage properties. Functionalization of CNTs can be done with groups such as carboxyl groups [43], alkyl groups [44], amide groups [45], hydroxyl groups [30]. Fig. 2 shows FTIR spectra of MWCNT samples functionalized with hydroxyl and carboxyl groups. The spectra of functionalized MWCNTs exhibit different bands from those of MWCNT. FTIR spectrum of pure MWCNT does not show any peaks belonging to organic or inorganic chemical groups. The peaks at 1570 and 1736 cm^{-1} are attributed to the C=C bonds of aromatic rings on the MWCNT walls [46,47]. This provides information about the surface properties and chemical structures of CNTs, while also revealing that the pure forms of these materials are devoid of certain chemical groups.

In the spectrum of MWCNT-OH, a broad peak around 3432 cm^{-1} is attributed to the O–H stretching vibration due to hydrogen bonding, while the peak near 1190 cm^{-1} corresponds to the bending vibration of the hydroxyl group. It is seen that the intensity of these peaks increases in the spectrum, which indicates that the amount of hydroxyl groups increases as a result of the oxidation of MWCNTs with H_2O_2 in

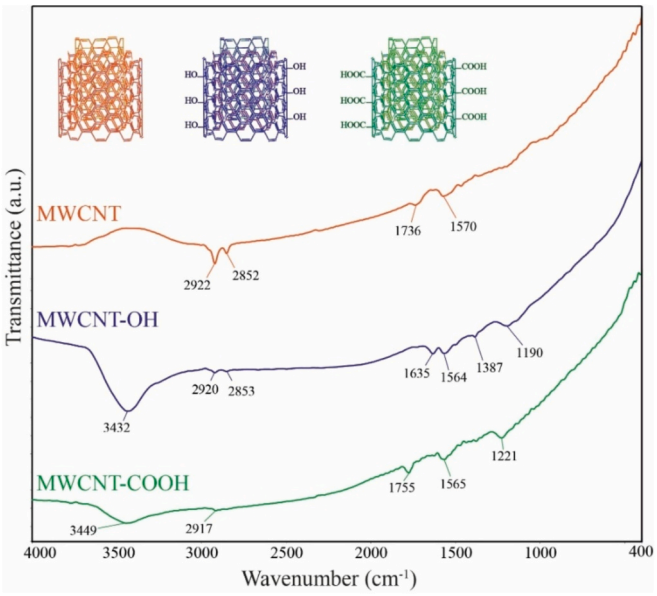

Fig. 2. FTIR spectra of MWCNT and functionalized MWCNTs.

$FeCl_24H_2O$ solution. The peak at 1635 cm^{-1} represents the conjugated C=C structure in the graphene structure of MWCNTs. This peak shows that the structural integrity of MWCNTs is preserved and still exists after oxidation [39].

In the spectrum of MWCNT oxidized with a mixture of sulfuric acid and nitric acid, various peaks were observed at certain wavenumbers. The peak at 1221 cm^{-1} indicates the vibration stretching of –C–O groups; the peak at 1565 cm^{-1} indicates the asymmetric stretching of –COO; the peak in the range of 1755 cm^{-1} indicates the stretching of C=O groups; the peak at 2917 cm^{-1} indicates the asymmetric and symmetric stretching of C–H groups; and the peak at 3449 cm^{-1} indicates the stretching of O–H groups. Especially the peak at 1565 cm^{-1} shows that oxygen-containing functional groups were added to CNTs during acid treatment. These findings suggest that acid oxidation changes the surface chemistry of MWCNTs and oxygen-containing groups are attached in this process [48–50].

3.1.2. Raman analysis

Raman spectroscopy is a powerful tool for characterizing carbon nanotubes (CNTs) and their functionality. This technique is particularly useful for studying the structure, defects and functional groups and other structural features of nanotubes [51,52]. Fig. 3 shows the Raman spectra of MWCNT, MWCNT-OH and MWCNT-COOH structures.

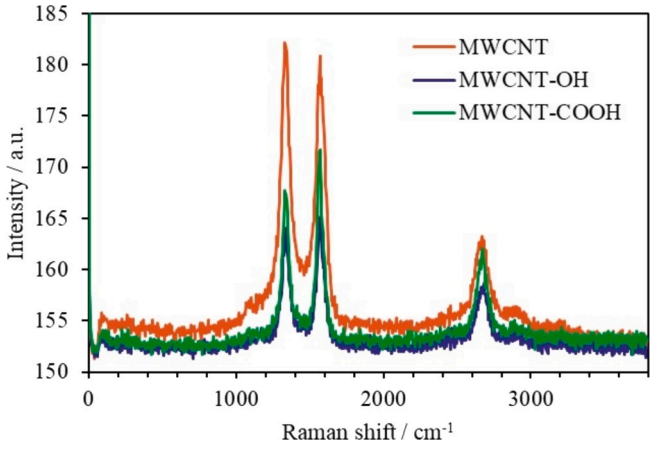

Fig. 3. Raman spectra of MWCNT, MWCNT-OH and MWCNT-COOH.

MWCNT has a D band around 1332 cm^{-1}. This band is associated with the presence of defects in the structure of carbon nanotubes. The G band, which appears around 1586 cm^{-1}, is due to the vibrations of the carbon–carbon bonds and is usually associated with a healthy, flawless graphite or carbon structure. The 2D band is observed around 2669 cm^{-1}. This band usually occurs in the presence of multiple functional groups or defects. In the case of MWCNT-OH, D, G and 2D bands were observed at 1340, 1568 and 2679 cm^{-1}, respectively, while in the case of MWCNT-COOH, they were observed at 1331, 1568 and 2668 cm^{-1}. Again, when the band intensities of the Raman spectra are examined, it is seen that they are different from each other. The changes in the locations and intensities of the D, G and 2D bands indicate that some changes have occurred in the structure of the MWCNT with functionalization, but the structure has not been significantly deteriorated. Because it is seen that none of the D, G and 2D bands are lost.

3.1.3. TG analysis

The thermal properties of functionalized MWCNT were investigated by thermogravimetric analysis. In this study, functional groups such as hydroxyl and carboxyl bonded to the structure can be removed from the structure by decomposition at different temperatures with the following reactions.

$$MWCNT-OH \rightarrow MWCNT-H+CO_g \quad (1)$$

$$MWCNT-COOH \rightarrow MWCNT-H+CO_{2(g)} \quad (2)$$

Fig. 4 shows the TG thermograms of MWCNT, MWCNT-OH and MWCNT-COOH and the thermal stability parameters calculated from these thermograms in Table 1. In general, the mass loss occurring between room temperature and 150 °C is related to the release of physically adsorbed water on the surface. This provides information about the moisture content of the material. Dehydration of functional groups and their degradation reactions are observed between 150 °C and 600 °C [53,54]. When the thermograms of MWCNT, MWCNT-OH and MWCNT-COOH are examined, it is seen that 2.1, 0.5 and 1.6 wt% mass loss occurs at 87, 91 and 146 °C, respectively. This is thought to be due to the adsorption of moisture in the atmosphere [39]. From the thermograms of MWCNT-OH and MWCNT-COOH, it was observed that the degradation of hydroxyl and carboxyl groups occurred at 361 and 478 °C with a mass loss of 1.9 and 2.6 wt%, respectively. Finally, the degradation of MWCNT, MWCNT-OH and MWCNT-COOH at 770, 838 and 812 °C resulted in mass losses of 16.7, 26.6 and 32.9 wt%, respectively. When the results were evaluated as a whole, it was seen that the total mass losses for MWCNT, MWCNT-OH and MWCNT-COOH were 80.0, 69.6 and 60.8 %. It was observed that the mass loss increased in proportion to the molecular weights of the groups attached to the structure with functionalization. This shows the changes in the chemical structure of MWCNT and the degradation of certain functional groups. In addition, with functionalization, the decomposition temperature of MWCNT at 770 °C shifted to higher temperatures. This result shows that MWCNT became more thermally stable with functionalization.

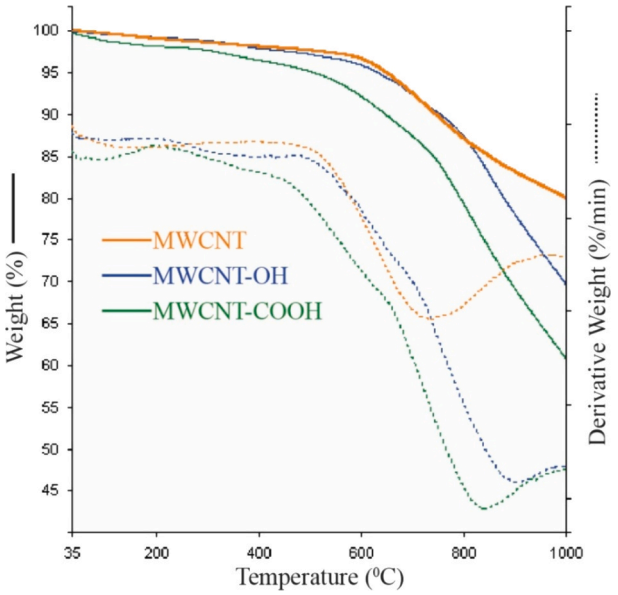

Fig. 4. TG/d[TG] thermograms of MWCNT and functionalized MWCNTs.

Table 1
Thermal stability parameters of MWCNT and functionalized MWCNTs.

Samples	T_{max1} (°C)	Delta Y_1 (%)	T_{max2} (°C)	Delta Y_2 (%)	T_{max3} (°C)	Delta Y_3 (%)	Residue (%)
MWCNT	87	2.1	–	–	770	16.7	80.0
MWCNT-OH	91	0.5	361	1.9	838	26.6	69.6
MWCNT-COOH	146	1.6	478	2.6	812	32.9	60.8

3.1.4. TEM images

TEM is a powerful tool for characterizing MWCNTs. TEM images of MWCNT and MWCNT-OH samples at the same magnification ratio are given in Fig. 5. The diameters of MWCNT and MWCNT-OH are in nanoscale, while their lengths are in micrometers. The average inner diameters of MWCNT and MWCNT-OH samples vary between 2.5–7 nm and their outer diameters vary between 8–16 nm. The difference between the inner and outer diameters indicates that the carbon nanotube samples are multi-walled. Morphological changes such as capping at the ends of MWCNT were also observed with oxidation. This shows that the internal structure and chemical properties of the nanotubes change [55]. It can be said that the hydrophilic property of MWCNT increases with functionalization and as a result, van der Waals interactions and agglomeration between carbon nanotubes decrease. Because in the TEM images of MWCNT-OH, functionalized MWCNTs are seen to have a better dispersed and separated structure. This provides better dispersion of the nanotubes and therefore better performance.

3.1.5. SEM/EDX analysis

FTIR, TG and TEM analyses show that the functionalization process significantly affects the surface properties and distribution of MWCNTs. The changes in the morphological properties and elemental composition of the samples are explained by the SEM/EDX technique. Fig. 6 shows both SEM and EDX results of the samples at the same magnification ratio. The morphology of the MWCNT samples exhibits an agglomerated and rather rough structure before modification. With functionalization, it was observed that the MWCNTs (e.g., MWCNT-OH or MWCNT-COOH) showed less aggregation and rough surface and exhibited a more homogeneous distribution. In addition, the functionalized MWCNTs have a more pronounced tubular surface morphology. These results are in good agreement with the TEM images. EDX analysis shows that the carbon content of the samples decreases and the oxygen content increases with functionalization, similar to thermogravimetric analyses (Table 2). These results prove that the MWCNT surface is functionalized with hydroxyl and carboxyl groups. Another analysis technique that shows the presence of hydroxyl and carboxyl groups in the structure of MWCNT by oxidation reaction is FTIR. There is no hydroxyl peak around 3500 in the structure of pure MWCNT. An intense and widespread hydroxy peak was observed at 3432 cm^{-1} by hydroxylation reaction. In addition, the band that emerged at 3449 cm^{-1} by carboxylation reaction shows the hydroxyl peak of the carboxyl group, the band at 1221 cm^{-1} shows the C-O band and the band at 1755 cm^{-1} shows the C=O band. These results are also in good agreement with the EDX and thermal analysis results.

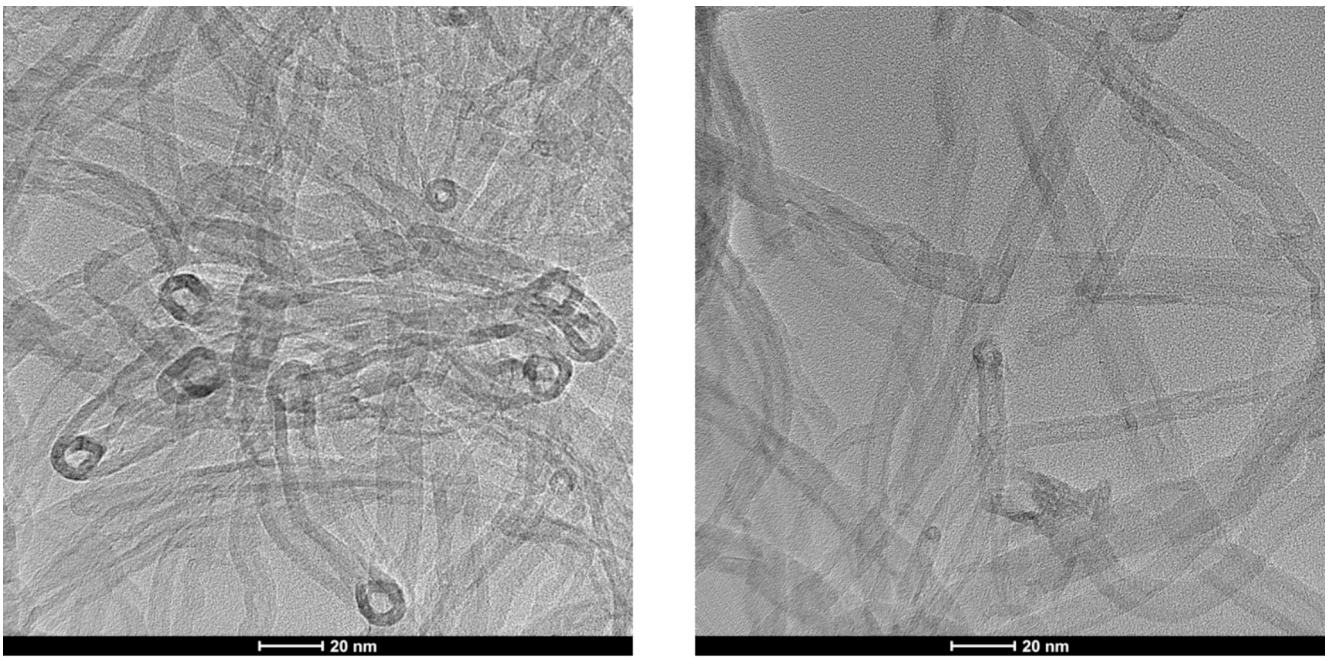

Fig. 5. TEM images of a) MWCNT and b) MWCNT-OH.

3.1.6. AFM images

Atomic force microscopy (AFM) was used to investigate the structure and surface topography of carbon nanotubes. Fig. 7 shows the topographic and three-dimensional topographic micrographs of MWCNT, MWCNT-OH and MWCNT-COOH structures. It is possible to observe the presence of irregularly shaped particles and filamentous structures (carbon nanotubes) from the three-dimensional images. It is seen that the roughness increases with the functionalization of MWCNT. Because the roughness values for MWCNT, MWCNT-OH and MWCNT-COOH structures were calculated as 10.33, 13.03 and 17.85 nm, respectively. Again, it is seen in the 3D images of the samples that their heights also change with functionalization. For example, the heights of MWCNT, MWCNT-OH and MWCNT-COOH structures were measured as 71.4, 72.5 and 84.7 nm, respectively. These results show that functionalization of MWCNT results in significant changes in its topography and surface roughness.

3.2. Hydrogen storage

The functionalization of MWCNT can affect their hydrogen storage capacity. Fig. 8 shows the storage capacities of MWCNT, MWCNT-OH and MWCNT-COOH samples as a function of pressure at cryogenic temperature. Hydrogen adsorption on carbon nanotubes occurs primarily at three main sites: the exterior surface, the interior surface, and the interstitial spaces within the nanotube structure. On the exterior surface, hydrogen molecules are adsorbed primarily through van der Waals forces, allowing for weak but effective interactions. The interior surface offers additional points for adsorption, where hydrogen can occupy narrow gaps within the nanotube. Additionally, the interstitial spaces provide opportunities for hydrogen molecules to be captured in the voids between carbon atoms. Overall, the combination of these adsorption sites enable efficient hydrogen uptake [56]. The storage capacity of MWCNT initially increases rapidly with increasing pressure, decreases without reaching a plateau as the pressure is increased, and the storage capacities increase again when the pressure is increased. A similar situation was observed for the storage of hydrogen on activated carbon surfaces produced from almond shells and tangerine peel [29,57]. The observation of a maximum point in the isotherm curve is explained by the term excess adsorption. Excess adsorption refers to the accumulation of adsorbed gas molecules on the surface of a material at a certain temperature and pressure, more than the theoretically expected maximum capacity. Excess adsorption may be i. when the interactions between the molecules on the surface cause the adsorbed molecules to bind more strongly to the surface and ii. when the pore structure of the material causes the molecules to be squeezed into more space, thus resulting in greater adsorption capacity [17,29]. In the cases of MWCNT-OH and MWCNT-COOH, the adsorbed amount of hydrogen initially increases rapidly with increasing pressure, the isotherm curve reaches a plateau when the pressure is continued to be increased, and when the pressure is further increased, it is seen that the amount of adsorbed hydrogen increases. In this case, it can be said that multilayer adsorption occurs. This result shows that functionalization causes significant changes in the surface properties of MWCNT. Van der Waals interactions are in question between carbon nanotube molecules [41]. The increase in the storage capacity of the samples with increasing pressure is a result of the increase in the density of gas molecules and increased van der Waals interactions [57].

Functionalized samples have higher storage capacities. There may be several reasons for this increase. Functional groups can establish stronger chemical interactions with hydrogen. These interactions can increase the storage capacity by allowing hydrogen to bind more tightly to the nanotube surface. Functionalization can increase the surface reactivity of CNTs, allowing hydrogen to be better adsorbed. For example, functional groups containing oxygen or nitrogen can increase the ability of hydrogen to bind to the nanotube surface. Functional groups can affect the physical and chemical adsorption mechanisms of hydrogen. This has a direct effect on the way hydrogen is stored and thus can affect the total storage capacity [58]. A similar situation was observed for the adsorption of hydrogen on functionalized and Schiff base based multi-walled carbon nanotubes. In the study, it was stated that functionalization increased the hydrogen storage capacity by creating new chemical groups on the surface of carbon nanotubes.

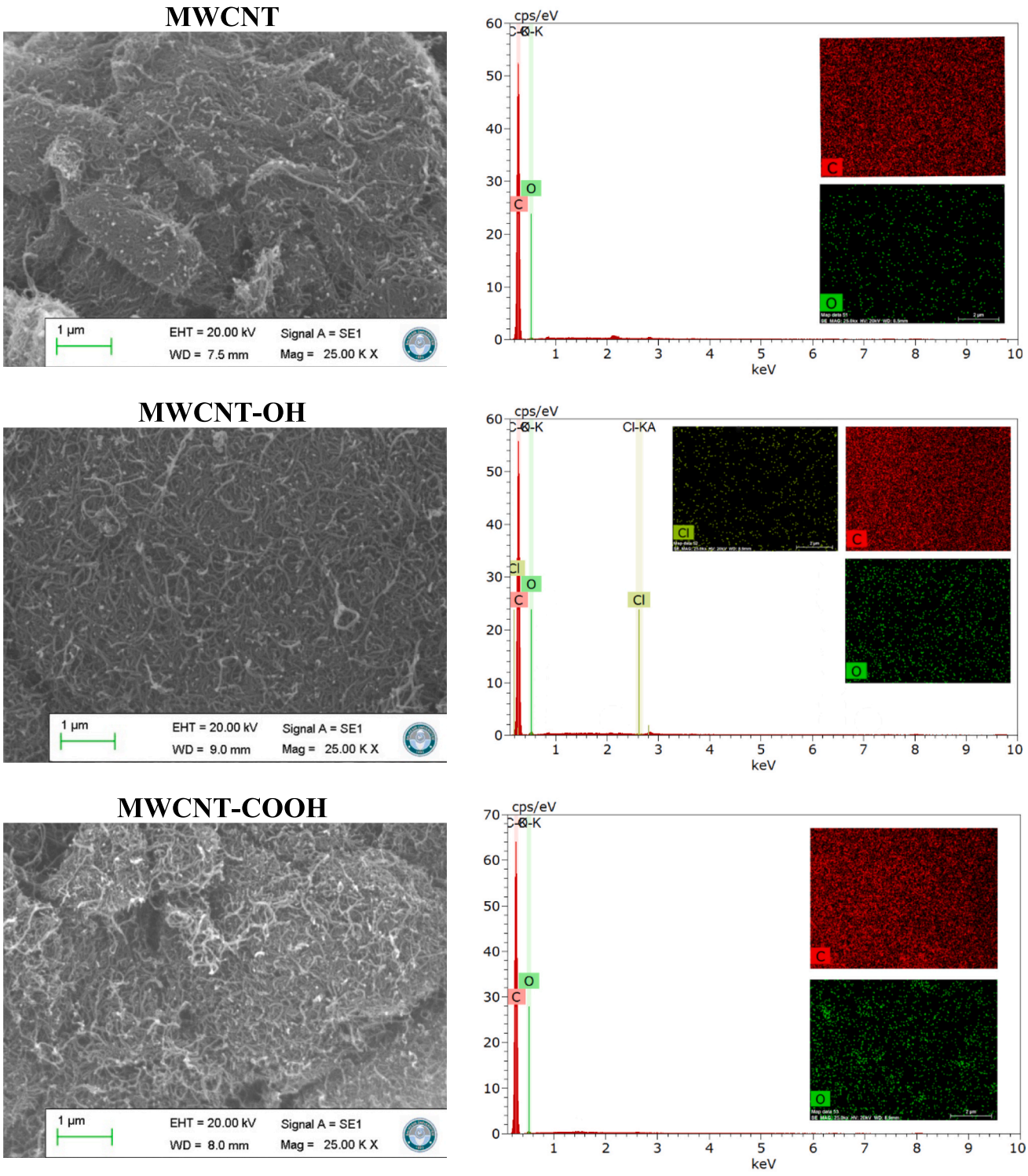

Fig. 6. SEM images of MWCNT and functionalized MWCNTs.

Table 2
EDX elemental content of MWCNT and functionalization MWCNTs.

Samples	Elements (wt. %)		
	C	O	Cl
MWCNT	96.1	3.9	–
MWCNT-OH	93.1	5.7	1.2
MWCNT-COOH	92.4	7.6	–

Especially functional groups such as –OH and C–N increased the binding ability by providing stronger electrostatic and London dispersion interactions with hydrogen molecules. These groups enabled hydrogen to interact more easily with the nanotube surface, which increased the adsorption capacity [39]. One of the most important parameters affecting the storage capacity of adsorbents is the BET surface area and pore volume. Fig. 9 shows the adsorption–desorption isotherm plots to obtain the pore size distribution profiles. The results are presented in Table 3. BET surface areas of MWCNT, MWCNT-OH and MWCNT-COOH

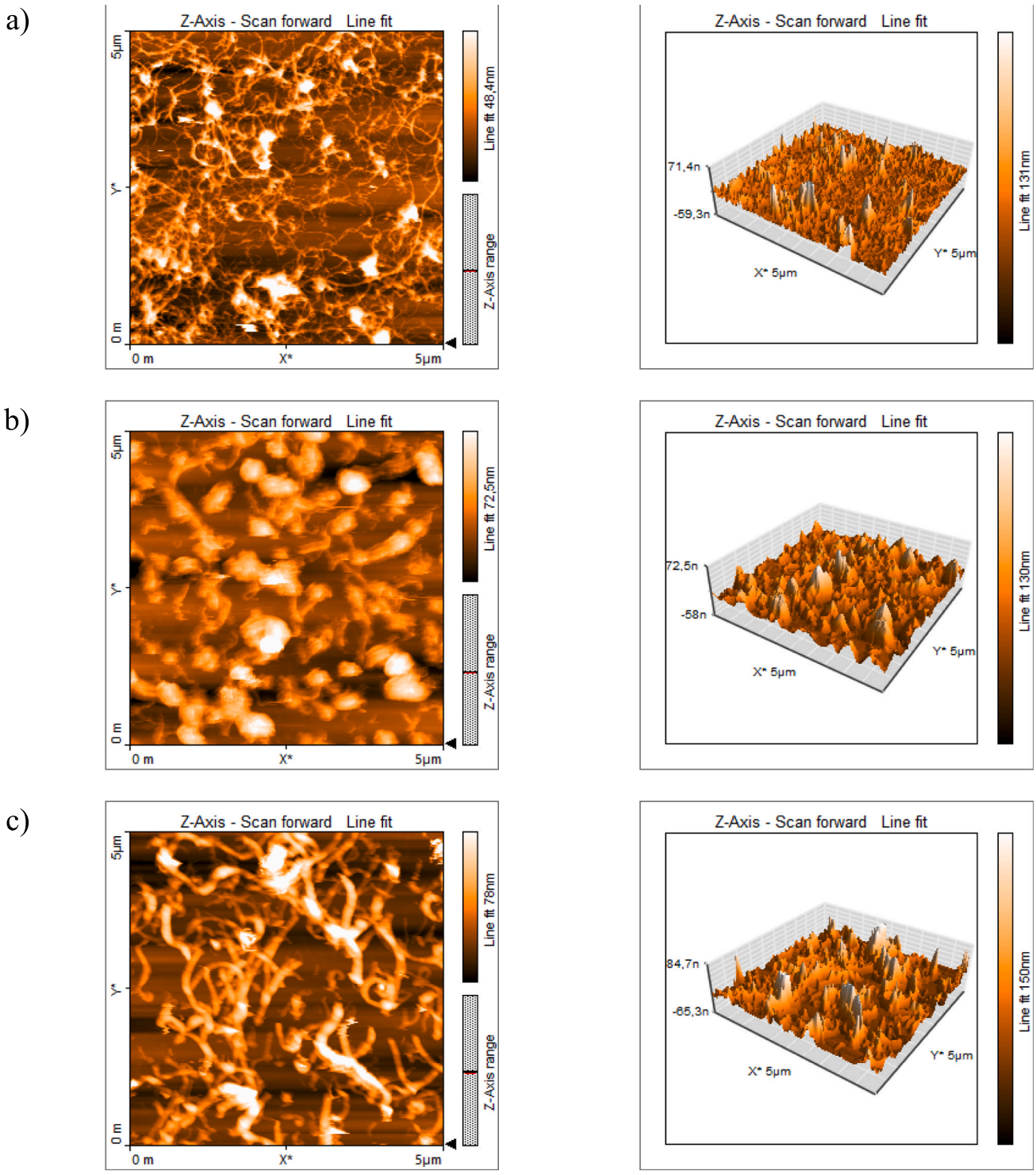

Fig. 7. AFM topographies of (a) MWCNT (b) MWCNT-OH (c) MWCNT-COOH samples.

are 271, 247 and 199 m^2/g, respectively. BET surface areas of MWCNT samples decrease with functionalization. The reasons for this decrease are: i. during functionalization, chemical groups can bind to the surface of MWCNT and cover the empty spaces on the surface of nanotubes, reducing the total surface area, ii. it may be due to aggregation, iii. it may be due to the blockage of the voids in the porous structure of MWCNT with the addition of functional groups, and iv. it may be due to defective points in the structure of MWCNT as a result of some chemical reactions during functionalization. The hydrogen storage capacities of the samples generally vary in direct proportion to the BET surface area. In the study, the hydrogen storage capacities of the samples increase with functionalization, while their BET surface areas decrease. In this case, it does not seem possible to explain the changes in the hydrogen storage capacity of the samples with the BET surface area. It is stated in the literature that the hydrogen storage capacity of the samples changes in direct proportion to the pore volume rather than the BET surface area [39]. Fig. 10 shows the change in the pore diameter of the samples with the cumulative pore volume. Table 3 and Fig. 10 show that the MWCNT samples do not have micropore volume and consist of meso and macropores. The meso and macropore volumes of MWCNT, MWCNT-OH and

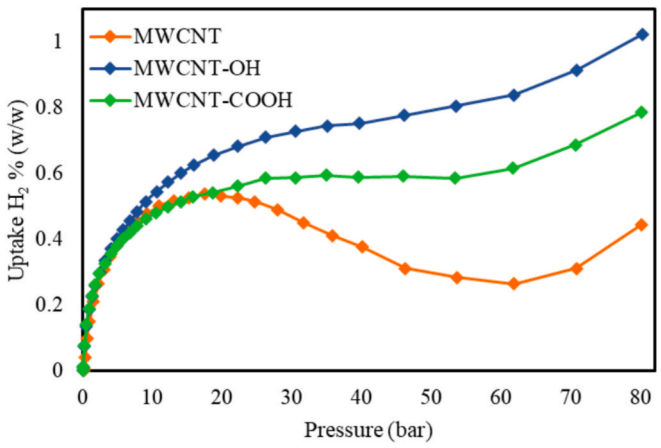

Fig. 8. Hydrogen adsorption isotherms of MWCNT, MWCNT-OH and MWCNT-COOH.

MWCNT-COOH samples are 0.496 and 0.083 cc/g, 1.209 and 0.781 cc/g, and 0.945 and 0.378 cc/g, respectively. These results show that MWCNT-OH has the highest meso and macro pore volume, followed by MWCNT-COOH and MWCNT, respectively. Parallel to the pore volume data, the sample with the highest hydrogen storage capacity is MWCNT-OH, followed by MWCNT-COOH and MWCNT. These results show that the increase in hydrogen storage capacity with functionalization changes directly proportional to the pore, especially the mesopore volume, rather than the BET surface area. The hydrogen storage capacities of MWCNT, MWCNT-OH and MWCNT-COOH samples at 1 and 10 bar

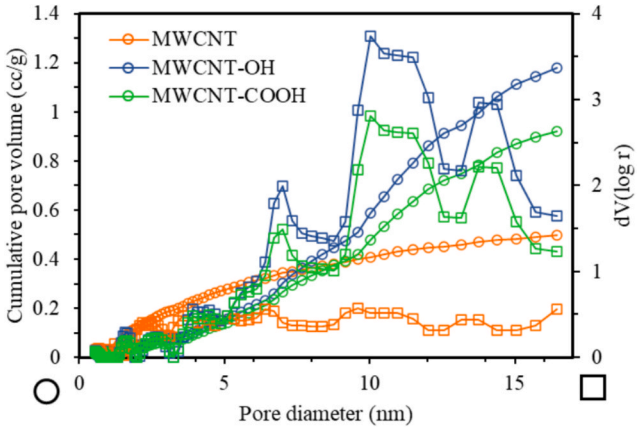

Fig. 10. Pore size distributions of carbon nanotubes.

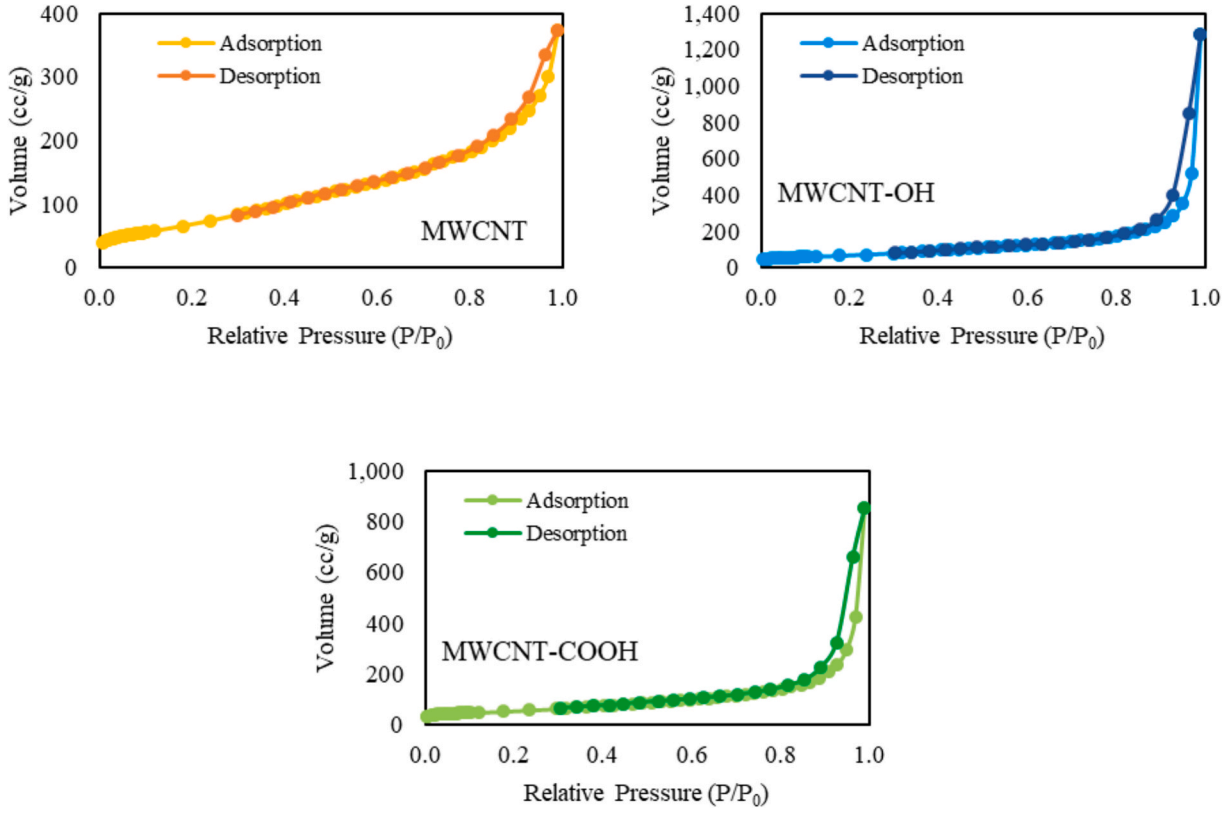

Fig. 9. N_2 adsorption–desorption isotherm curves of carbon nanotubes.

Table 3
BET surface areas and pore volumes of carbon nanotube samples.

Samples	H_2 % (w/w) (1 bar)	H_2 % (w/w) (10 bar)	Maximum value		S_{BET} (m^2/g)	V_t (cc/g)	V_{micro}(cc/g)	V_{meso} (cc/g)	V_{macro} (cc/g)
			H_2 % (w/w)	Pressure (bar)					
MWCNT	0.212	0.502	0.537	18	271	0.579	–	0.496	0.083
MWCNT-OH	0.226	0.514	1.023	80	247	1.990	–	1.209	0.781
MWCNT-COOH	0.228	0.461	0.786	80	199	1.323	–	0.945	0.378

and the pressure values at which maximum storage occurs are given in Table 3. The hydrogen storage capacities of MWCNT, MWCNT-OH and MWCNT-COOH at 1 and 10 bar are 0.212 and 0.502 wt%, 0.226 and 0.514 wt%, and 0.228 and 0.461 wt%, respectively. The pressures at which maximum removal occurs for MWCNT, MWCNT-OH and MWCNT-COOH samples are 18 bar (0.537 %), 80 bar (1.023 %) and 80 bar (0.786 %), respectively.

3.3. Adsorption rate

Adsorption processes are affected by various parameters such as particle size, initial concentration, pH, adsorbent amount and contact time [59]. Especially for hydrogen adsorption, pore size, pressure and contact time are critical factors [60]. Fig. 11 shows the adsorbed amounts of MWCNT, MWCNT-OH and MWCNT-COOH samples with time at 77 K. The adsorbed amount of hydrogen shows a rapid increase at the beginning. During this period, gas molecules collide the adsorbent surface and adsorb rapidly. At this stage, the adsorbed amount increases proportionally with time. As time progresses, the empty areas on the adsorbent surface decrease and the probability of molecules reaching the surface decreases. Therefore, the adsorption rate slows down and the adsorbed amount reaches saturation at a certain point. When the saturation point is reached, the adsorbed amount remains constant because all active sites on the surface are filled. At the saturation point, an equilibrium occurs between the adsorption and desorption processes. In this case, the adsorbed amount does not change with time, but some of the molecules on the surface may be released, while others may be adsorbed back to the surface. The adsorption process is generally based on an equation such as the following:

$$\frac{dy}{dt} = R_a - R_d \tag{3}$$

Here, dy/dt: change in adsorbed amount with time, R_a: adsorption rate and R_d: desorption rate. The adsorption rate of hydrogen can be related to the pressure and surface coverage fraction. For example, the adsorption rate increases proportionally with the pressure, which causes the adsorbed amount to increase with time. Mathematically, the adsorption rate of hydrogen can be expressed as:

$$R_a = K_a \bullet p \bullet (1 - y) \tag{4}$$

Here, K_a is the adsorption constant, p is the pressure and y is the surface coverage fraction [61]. According to this equation, as the pressure increases, the adsorption rate also increases, which leads to more hydrogen being adsorbed onto the surface. As a result, as the pressure increases, the amount of hydrogen adsorbed also increases, which has a significant effect on the adsorption kinetics. The desorption rate, depending on the amount adsorbed, is expressed as follows:

$$R_d = K_d \bullet y \tag{5}$$

It is stated that the time for hydrogen adsorption to reach equilibrium may vary depending on the pore size of the adsorbent [60]. All three CNT samples used in the study are mesoporous. When the figures are examined, it is seen that the adsorption process reaches equilibrium in approximately 2 min. Fig. 11 also shows the change of the amount adsorbed on all CNT surfaces at three different pressures with time. As the pressure increases, the density of gas molecules increases. This causes the molecules to collide with the adsorbent surface more frequently. More collisions increase the adsorption rate because the probability of molecules reaching the surface increases. High pressure allows more molecules to be held on the adsorbent surface.

3.4. Adsorption kinetics

Adsorption kinetics is very important to understand adsorption processes and pseudo-first order and pseudo-second order models are

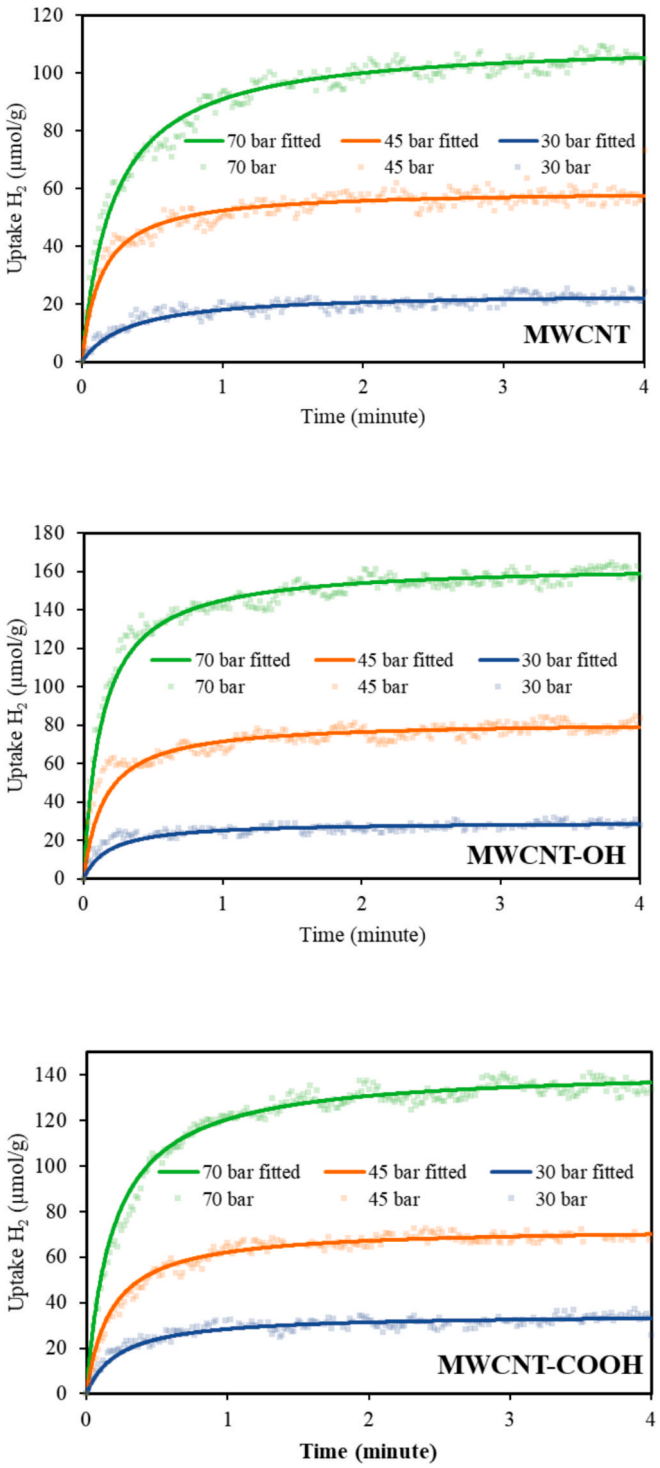

Fig. 11. The change of the adsorbed hydrogen amount on the surfaces of MWCNT and functionalized MWCNTs at different pressures with time.

widely used [62,63]. These models are derived from chemical reaction kinetics are applied to time-dependent adsorption data [62]. Pseudo-first and second order integrated rate equations were used to analyze the experimental data in the study.

The pseudo-first-order kinetic model is a widely used approach to describe the adsorption process where the rate of adsorption is proportional to the difference between the equilibrium concentration and the concentration at time t. This model is particularly applicable when the concentration of the adsorbate is relatively low compared to the

adsorption capacity of the adsorbent. Pseudo-first order integral rate expression;

$$\ln(q_e - q_t) = \log q_e - k_1 t \quad (6)$$

Where q_t is the amount of adsorbate adsorbed at time t (μmol/g), q_e is the amount of adsorbate adsorbed at equilibrium (μmol/g), k_1 is the pseudo-first-order rate constant (min^{-1}) and t is time (min). In this equation, q_e and q_t represent the amounts of adsorbate (hydrogen in this case) adsorbed on the adsorbent at equilibrium and at a certain time t, respectively. According to this equation, the value of the pseudo-first-order rate constant k_1 can be determined from the slope of the plot of $\ln(q_e - q_t)$ versus t [64]. The regression coefficient values obtained by applying the experimental data to the pseudo-first-order integral rate expression are given in Table 4.

The pseudo-second-order kinetic model is commonly used to describe the adsorption process where the rate of adsorption is proportional to the square of the amount of adsorbate already adsorbed. This model is particularly applicable when the adsorption capacity is high and the adsorption sites are not fully occupied. The pseudo-second-order integrated rate equation can be expressed as:

$$\frac{t}{q_t} = \frac{1}{k_2 q_e^2} + \frac{t}{q_e} \quad (7)$$

Where k_2 is the pseudo-second-order rate constant (g/(μmol·min)). This equation indicates that a plot of t/q_t versus t will yield a straight line, where the slope of the line is $1/q_e$ and the intercept is $1/k_2 q_e^2$ [65]. The regression coefficient values obtained by applying the kinetic data to the pseudo second-order integrated rate expression are given in Table 4.

The regression coefficient values calculated for the pseudo first order integrated rate expressions are in the range of 0.5830–0.7987, while those for the pseudo second order integrated rate expressions are in the range of 0.9845–0.9978. The regression coefficient values calculated for the pseudo second order equations are higher. This result shows that the experimental data are compatible with the pseudo second order integrated rate equation. Table 4 also shows $q_{e(cal)}$, $q_{e(exp)}$ and k_2 values calculated for the pseudo second order equation. The second way to test the compatibility of the experimental data with the pseudo second order equation is to compare $q_{e(cal)}$ and $q_{e(exp)}$ values. When the values in Table 4 are compared, it can be said that $q_{e(cal)}$ and $q_{e(exp)}$ data are in very good agreement with each other. This result proves that the experimental data are compatible with the pseudo second order equation. The plots obtained by applying the kinetic data to the pseudo second-order integrated rate expression are given in Fig. 12. Again, the fitting curves obtained by using the data obtained from the pseudo second-order rate expressions are shown in Fig. 11. It can be said that the experimental data are in very good agreement with the fitting curve. In the literature, the experimental kinetic results for hydrogen adsorption on the defective fullerene surface showed a rapid initial adsorption phase followed by a slower stabilization to equilibrium. At lower pressures, the adsorption rate was higher, with the D-C60-1 h-500 rpm sample achieving a significant rate constant of 8.03 μmol/g min at 25 bar. As pressure increased, the adsorption rate decreased due to surface saturation effects. The kinetic analysis demonstrated that the adsorption process followed a pseudo-second-order model. These findings indicate that the processing conditions significantly influence the hydrogen storage capabilities of defective fullerenes [66].

Although pseudo-second-order kinetics is often linked to chemisorption processes, its applicability in this study is attributed to the surface-limited and structured nature of physical adsorption. Hydrogen, being a small, non-polar, and weakly interactive gas, primarily undergoes physisorption on carbon surfaces. This is supported by the rapid equilibrium time (~2 min), relatively low adsorption capacity, and the absence of activation energy barriers typical of chemisorption. The introduction of polar –OH and –COOH groups on MWCNT surfaces enhances the physisorption potential by increasing surface polarity and available interaction sites. As a result, the hydrogen uptake becomes more regulated by surface diffusion and site accessibility, rather than purely by Van der Waals forces. The high correlation ($R^2 > 0.99$) observed with the pseudo-second-order kinetics model thus reflects a surface-controlled physisorption mechanism, where the adsorption rate depends on the number and distribution of accessible surface sites rather than strong chemical bonding. Therefore, the dominance of the pseudo-second-order kinetics model in this case is mechanistically consistent with a structured, site-specific physisorption process rather than true chemisorption.

3.5. Adsorption mechanism

Determination of the rate limiting step in the adsorption process is very important for industrial applications. Because in mobile applications, the release and time of the stored gas are important. Depending on whether the adsorbate gas is stored on the solid surface or in the pores of the adsorbent, the adsorption mechanism can be external diffusion and/or intraparticle diffusion. Linear Boyd equation derived for adsorption of adsorbate on the surface of the adsorbent

$$\ln\left(1 - \frac{q_t}{q_e}\right) = -Rt + A \quad (8)$$

In this equation, R and A are known as the rate constant and the Boyd equation constant, respectively. According to the equation (8), the plot of $\ln(1\text{-}q_t/q_e)$ against t should give a straight line with slope −R and extrapolation A. The correlation coefficient values for the Boyd equation are given in Table 4. The correlation coefficient values in Table 4 are quite low. The relatively low regression coefficients suggest that external surface diffusion is not the rate-limiting step of hydrogen adsorption in these systems.

The Avrami equation is a model generally used to model kinetic processes such as crystallization, decomposition, intercalation and phase transformation, and especially to describe the rates of adsorption

Table 4
The kinetic parameters for hydrogen adsorption on MWCNT and functionalized MWCNTs.

Samples	Pressure (bar)	Pseudo-first order R^2	Pseudo-second order				Boyd R^2	Weber-Morris				Avrami		
			R^2	$q_{e(exp)}$ (μmol/g)	$q_{e(cal)}$ (μmol/g)	k_2		R_1^2	k_1	R_2^2	k_2	R^2	n	K_{Av}
MWCNT	70	0.7987	0.9969	109.5	111.1	0.040	0.6117	0.9504	106.10	0.7706	20.22	0.8057	0.4678	1.6502
	45	0.5914	0.9933	64.0	59.5	0.122	0.4801	0.9328	80.87	0.6103	8.96	0.8148	0.3665	1.5545
	30	0.6371	0.9718	26.7	23.9	0.131	0.5941	0.8707	22.28	0.6039	4.92	0.9045	0.5323	1.0635
MWCNT-OH	70	0.7684	0.9978	164.9	163.9	0.046	0.4789	0.9866	230.11	0.8253	20.74	0.7113	0.2903	1.9701
	45	0.6020	0.9935	84.6	81.9	0.082	0.5346	0.9856	137.19	0.7405	13.23	0.7372	0.3478	1.7996
	30	0.5830	0.9845	33.1	29.6	0.187	0.4735	0.9678	49.27	0.5597	4.37	0.8574	0.4191	1.3800
MWCNT-COOH	70	0.6958	0.9974	140.8	142.8	0.038	0.5105	0.9906	154.10	0.7213	18.22	0.8121	0.4093	1.7489
	45	0.6642	0.9963	75.9	73.0	0.078	0.5038	0.9775	82.89	0.6172	10.10	0.8824	0.5062	1.4999
	30	0.6337	0.9847	37.9	34.9	0.124	0.5472	0.9317	39.22	0.5433	5.80	0.8825	0.5522	1.2915

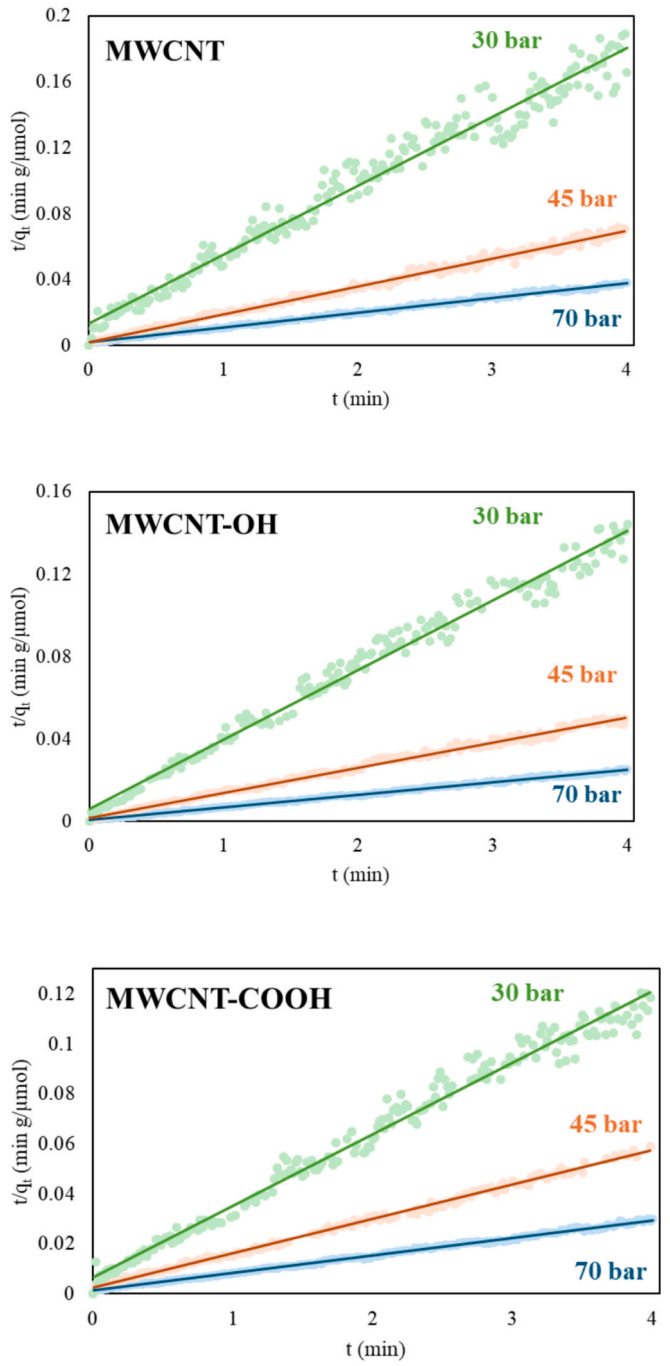

Fig. 12. The plots of t/q_t against t for hydrogen adsorption on the surfaces of carbon nanotubes at different pressures.

or desorption events [67]. Avrami equation can be given as following:

$$-\ln(1-\theta) = k_{AV}t^{n} \quad (9)$$

where θ is the conversion fraction; k_{AV} is the rate constant; t is time and n, Avrami parameter. The logarithmic form of this equation is as follows:

$$\ln[-\ln(1-\theta)] = \ln k_{AV} + n\ln t \quad (10)$$

For equation (10), the plot of ln[-ln(1-θ)] against lnt should give a straight line with slope n and extrapolation k_{AV}. The regression coefficient (R^2), k_{AV} and n values obtained by applying the experimental data to equation (10) are given in Table 4. If the Avrami equation gives a straight line passing through the origin and/or if the value of n is less than one, it can be said that the adsorption mechanism is diffusion controlled [68]. The experimental data do not give a straight line passing through the origin. However, the fact that the n values are below 1 supports a diffusion-limited adsorption mechanism rather than a purely surface reaction-limited process. This shows that the diffusion mechanism is the rate-determining step to a certain extent. Because the regression coefficients vary between 0.7113–0.9045, which limits the diffusion-controlled mechanism to some extent.

The intra-particle diffusion model is an approach used to explain the diffusion of gas inside the adsorbent. This model takes into account the movement of gas within the pore structure of the adsorbent and the factors affecting the rate of this movement. If the intra-particle diffusion process is the only rate-determining step, then according to the Weber-Morris model, the q_t versus $t^{1/2}$ curve should give a straight line through the origin. However, if the adsorption steps are independent of each other, the q_t versus $t^{1/2}$ curve contains two or more intersecting lines depending on the mechanism [69]. The Weber-Morris equation for intra-particle diffusion is given by the equation (11) [70,71].

$$q_t = k_{dif}\sqrt{t} + C \quad (11)$$

According to this equation, the plot of q_t versus $t^{1/2}$ should give a straight line with slope k_{dif} and extrapolation C. From Fig. 13, it can be seen that the plot of q_t versus $t^{1/2}$ is not a straight line through the origin. In this case, intraparticle diffusion is not the only rate-determining step. Fig. 13 shows the intraparticle diffusion curves for the Weber-Morris equation. Table 4 shows the model parameters for the corresponding equation. The curves show bilinearity. The first part of this linearity represents the diffusion of the adsorbate from the gas bulk phase to the adsorbent surface, and the second part represents the intraparticle diffusion of the adsorbate into the interior of the adsorbent [65]. When the k_1 and k_2 values in Table 4 are compared, k_2 values are lower. The diffusion rate of the gas depends on the pore size distribution of the adsorbent. Different pore sizes can affect the movement of the gas in different ways. Table 3 shows that the MWCNT and functionalized MWCNT samples do not have micropores and are largely composed of mesopores. The intra-particle diffusion model is observed in both microporous and mesoporous solids. Microporous solids are materials that generally have pore sizes smaller than 2 nm. Materials such as activated carbons and zeolites fall into this category [72,73]. In micropores, the diffusion of gas molecules occurs more slowly due to the narrow structure of the pores and the equilibrium period takes longer. Mesoporous solids are materials with pore sizes between 2 nm and 50 nm. Such pores can provide faster diffusion of gases because the pores are wider and provide more space for the movement of molecules [73]. As a result, the presence of two intersecting linear regions in the q_t vs. $t^{1/2}$ plot implies a two-step process: initial external surface adsorption followed by mesopore diffusion, which is consistent with the mesoporous structure revealed by BET analysis.

Experimental results show that the adsorption process is a rapid process and reaches equilibrium on the carbon nanotube surface and pores in about 2 min. This result shows that the adsorption process first occurs on the surface of the adsorbent and then by diffusion into the mesopores of the adsorbent. Fig. 14 shows the transfer of hydrogen molecules from the gas phase first to the outer walls of the MWCNT samples and then the intraparticle diffusion mechanism to the inner parts of the tubes. Again, the situation where hydrogen molecules are adsorbed in the gaps between the tubes is schematized. As seen from TEM analyses, the inner diameter of the MWCNT samples varies between 2.5–7 nm. This value shows that the gap in the inner parts of the MWCNTs correspond to the mesopore.

Table 5 compares the functionalized multi-walled carbon nanotubes (MWCNT-OH and MWCNT-COOH) synthesized in this study with various hydrogen adsorbents reported in the literature. The comparison focuses on parameters such as BET surface area, pore structure, hydrogen storage capacity, adsorption kinetics, and thermal stability.

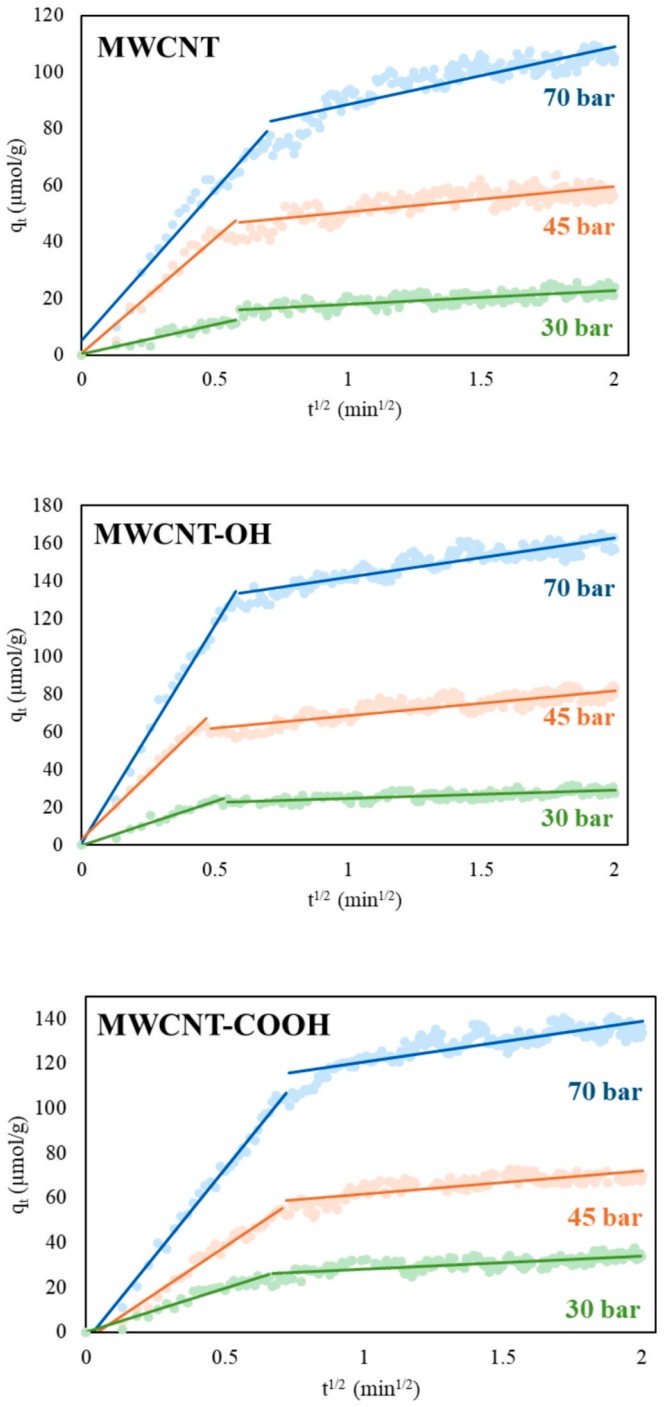

Fig. 13. The plots of q_t against $t^{1/2}$ for hydrogen adsorption on the surfaces of carbon nanotubes at different pressures.

The functionalized carbon nanotubes synthesized in this study offer significant advantages over other carbon-based adsorbents in the literature in many aspects such as better dispersed structure, high mesopore volume, stronger H_2 interaction groups, effective storage at high pressure and fast adsorption kinetics. It is one of the rare studies where functionalization increases the capacity by improving the pore structure and the mechanism is supported by detailed kinetic modeling.

3.6. Factors affecting the efficiency of hydrogen adsorption

The efficiency of hydrogen adsorption on MWCNT-based materials is governed by several interrelated parameters. One of the most influential factors is the type of surface functionalization applied to the nanotubes. The introduction of hydroxyl (–OH) and carboxyl (–COOH) groups significantly enhances adsorption by increasing the surface polarity and creating additional active sites for hydrogen interactions. These polar functional groups facilitate stronger physisorption through dipole-induced and dispersion forces, resulting in a noticeable increase in hydrogen uptake. Among the modified samples, MWCNT-OH displayed the highest storage capacity, demonstrating the effectiveness of hydroxyl functionalization. Another critical factor is the increase in mesopore volume following functionalization. While the BET surface area slightly decreased due to the occupation of surface sites by functional groups, the mesoporous and macroporous volumes increased considerably—most notably in MWCNT-OH. This enhanced pore structure enables multilayer adsorption and improves the diffusion of hydrogen molecules into the interior of the nanotubes, leading to improved overall storage efficiency. Operating pressure also plays a significant role in adsorption efficiency. Higher hydrogen pressures increase molecular density and collision frequency, which facilitates faster and more extensive adsorption on the nanotube surfaces. The highest storage capacities for all samples were observed at 80 bar, with MWCNT-OH achieving a maximum of 1.023 wt%. Additionally, the surface morphology and dispersion characteristics of the nanotubes influence their adsorption behavior. TEM and SEM analyses revealed that functionalized MWCNTs exhibit better dispersion and reduced agglomeration compared to pristine MWCNTs. This more uniform distribution increases the availability of accessible surface areas, thus contributing to improved adsorption performance. Finally, adsorption kinetics are a key determinant of efficiency. The hydrogen adsorption process reached equilibrium in approximately two minutes across all samples, reflecting a rapid and efficient mechanism. Kinetic modeling showed a strong agreement with the pseudo-second-order model, indicating that the process is primarily controlled by surface interactions typical of physisorption. Taken together, these findings reveal that the functionalization chemistry, pore structure, operating pressure, surface morphology, and adsorption kinetics collectively determine the efficiency of hydrogen adsorption in MWCNT-based materials.

4. Conclusions

In this study, pristine and functionalized multi-walled carbon nanotubes (MWCNTs) were synthesized and characterized to investigate their hydrogen adsorption behaviors. Surface functionalization with –OH and –COOH groups led to decreased BET surface area but increased mesopore volume and surface polarity. Characterization techniques including FTIR, Raman, TG, SEM/EDX, TEM, and AFM confirmed structural and morphological changes associated with oxidation. Hydrogen adsorption capacities improved with functionalization, especially in MWCNT-OH samples, correlating with enhanced surface hydrophilicity and reduced agglomeration. Kinetic modeling revealed that the adsorption process follows pseudo-second-order kinetics and primarily occurs via a physical adsorption mechanism, as supported by the rapid equilibrium time and diffusion-based model fits. Overall, the findings demonstrate that surface functionalization of MWCNTs significantly enhances hydrogen storage capacity through increased mesoporosity and surface polarity. Future studies should incorporate additional reference materials for broader comparative evaluations under identical conditions.

Declaration of competing interest

The author declares that they have no known competing financial interests or personal relationships that could have appeared to influence the work reported in this paper.

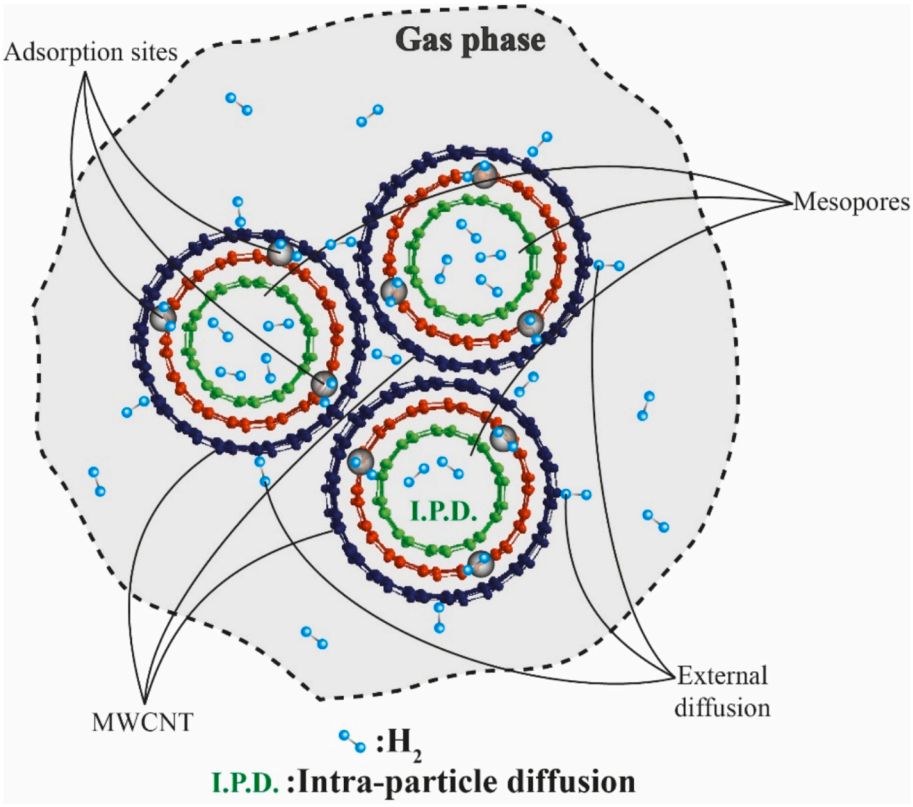

Fig. 14. Adsorption of hydrogen on the surface and pores of MWCNTs.

Table 5
Comparison of some properties of functionalized multi-walled carbon nanotubes synthesized in this study with adsorbents in the literature.

Criterions/ Properties	Literature	In this study	References
BET	Typically 500–1500 m^2/g (e.g., activated carbon)	MWCNT: 271, MWCNT-OH: 247, MWCNT-COOH: 199 m^2/g	[29,31,74]
Pore structure	Mostly microporous (<2 nm)	Mesoporous (2–50 nm); Vmeso: OH > COOH > pristine	[39]
Hydrogen storage capacity (wt%)	Mostly ≤ 1 wt%; e.g., 0.45–3.18 wt%	MWCNT-OH: 1.023 %, MWCNT-COOH: 0.786 %, MWCNT: 0.537 %	[29,30,31,37,38]
Functional Groups	Various: Schiff bases, metals, N/O groups	Hydroxyl (–OH) and Carboxyl (–COOH) functionalization	[30,39,58]
Thermal stability	Limited analysis	TGA shows thermal stability increased from 770 °C to 838 °C	[39]
Kinetic modeling	Mostly focused on capacity; limited kinetic studies	Pseudo-second-order + Boyd, Avrami, Weber-Morris models	[39,66]
Characterization	Typically FTIR and Raman	FTIR, Raman, SEM/EDX, TEM, AFM, DTA/TG	[30,58]
Pressure range	Usually 1–30 bar	Tested from 1 to 80 bar; max storage at 80 bar	[38]

Data availability

No data was used for the research described in the article.

References

[1] Sadorsky P. The effect of urbanization and industrialization on energy use in emerging economies: implications for sustainable development. Am J Econ Sociol 2014;73:392–409. https://doi.org/10.1111/ajes.12072.
[2] Assareh E, Delpisheh M, Farhadi E, Peng W, Moghadasi H. Optimization of geothermal-and solar-driven clean electricity and hydrogen production multi-generation systems to address the energy nexus. Energy Nexus 2022;5:100043. https://doi.org/10.1016/j.nexus.2022.100043.
[3] Kalair A, Abas N, Saleem MS, Kalair AR, Khan N. Role of energy storage systems in energy transition from fossil fuels to renewables. Energy Storage 2021;3:e135.
[4] Ang TZ, Salem M, Kamarol M, Das HS, Nazari MA, Prabaharan N. A comprehensive study of renewable energy sources: Classifications, challenges and suggestions. Energy Strategy Rev 2022;43:100939. https://doi.org/10.1016/j.esr.2022.100939.
[5] Badawi EY, Elkharsa RA, Abdelfattah EA. Value proposition of bio-hydrogen production from different biomass sources. Energy Nexus 2023;10:100194. https://doi.org/10.1016/j.nexus.2023.100194.
[6] Demirbaş A. Global renewable energy resources. Energy Source 2006;28:779–92. https://doi.org/10.1080/00908310600718742.
[7] Owusu PA, Asumadu-Sarkodie S. A review of renewable energy sources, sustainability issues and climate change mitigation. Cogent Eng 2016;3:1167990. https://doi.org/10.1080/23311916.2016.1167990.
[8] Doğan EE, Tokcan P, Kizilduman BK. Storage of hydrogen in activated carbons and carbon nanotubes. Adv Mater Sci 2018;18:5–16. https://doi.org/10.1515/adms-2017-0045.
[9] Edwards PP, Kuznetsov VL, David WI. Hydrogen energy, Philos Trans R Soc A Math Phys Eng Sci 2007;365:1043–56. https://doi.org/10.1098/rsta.2006.1965.
[10] Woods P, Bustamante H, Aguey-Zinsou KF. The hydrogen economy—Where is the water? Energy Nexus 2022;7:100123. https://doi.org/10.1016/j.nexus.2022.100123.
[11] Veziroglu TN. 21st Century's Energy: Hydrogen Energy System, In: J.W. Sheffield, Ç. Sheffield (Eds.), Assessment of Hydrogen Energy for Sustainable Development, NATO Sci. Peace Secur. Ser. C: Environ. Secur., Springer, Dordrecht, 2007, pp. 21–30. doi: 10.1007/978-1-4020-6442-5_2.
[12] Kim JW, Boo KJ, Cho JH, Moon I. Key challenges in the development of an infrastructure for hydrogen production, delivery, storage and use, In: Advances in Hydrogen Production, Storage and Distribution, Woodhead Publishing, 2014, pp. 3–31. doi: 10.1533/9780857097736.1.3.

[13] Yartys VA, Lototsky MV. An overview of hydrogen storage methods, hydrogen Mater. Sci Chem Carbon Nanomater 2005:75–104. https://doi.org/10.1007/1-4020-2669-2_7.

[14] Eberle U, Felderhoff M, Schüth F. Chemical and physical solutions for hydrogen storage. Angew Chem Int Ed 2009;48:6608–30. https://doi.org/10.1002/anie.200806293.

[15] Ni M. An overview of hydrogen storage technologies. Energy Explor Exploit 2006; 24:197–209. https://doi.org/10.1260/014459806779367455.

[16] Doğan ZS, Doğan EE, Bicil Z, Koçer Kizilduman B. The effect of Li-doping and doping methods to hydrogen storage capacities of some carbonaceous materials. Fuel 396 2025:135280. https://doi.org/10.1016/j.fuel.2025.135280.

[17] Lim KL, Kazemian H, Yaakob Z, Daud WW. Solid-state materials and methods for hydrogen storage: a critical review. Chem Eng Technol 2010;33:213–26. https://doi.org/10.1002/ceat.200900376.

[18] Zhang Y, Zhang W, Li B, Ren H, Qi Y, Zhao D. Effects of milling duration on electrochemical hydrogen storage behavior of as-milled Mg–Ce–Ni–Al-based alloys for use in Ni-metal hydride batteries. J Phys Chem Solids 2019;133:178–86. https://doi.org/10.1016/j.jpcs.2019.05.029.

[19] Heydariyan Z, Monsef R, Salem KH, Samimi F, Taha ZA, Salavati-Niasari M. Facile preparation and characterization of $SmMn_2O_5/Mn_2O_3$/g-$C3N_4$ nanocomposites for electrochemical hydrogen storage application. Int J Hydrogen Energy 2024;90: 1300–12. https://doi.org/10.1016/j.ijhydene.2024.10.075.

[20] Monsef R, Salavati-Niasari M. Tuning architectural synergy reactivity of nano-tin oxide on high storage reversible capacity retention of ammonium vanadate nanobelt array cathode for lithium-ion battery. Mater Sci Eng B 2024;310:117743. https://doi.org/10.1016/j.mseb.2024.117743.

[21] Kianpour G, Salavati-Niasari M, Emadi H. Sonochemical synthesis and characterization of NiMoO nanorods. Ultrason Sonochem 2013;20:418–24. https://doi.org/10.1016/j.ultsonch.2012.08.012.

[22] Behpour M, Ghoreishi SM, Gandomi-Niasar A, et al. The inhibition of mild steel corrosion in hydrochloric acid media by two Schiff base compounds. J Mater Sci 2009;44:2444–53. https://doi.org/10.1007/s10853-009-3309-y.

[23] Salavati-Niasari M, Davar F, Loghman-Estarki MR. Controllable synthesis of thioglycolic acid capped $ZnS(Pn)_{0.5}$ nanotubes via simple aqueous solution route at low temperatures and conversion to wurtzite ZnS nanorods via thermal decompose of precursor. J Alloys Compd 2010;494:199–204. https://doi.org/10.1016/j.jallcom.2009.10.265.

[24] Mohandes F, Salavati-Niasari M. Sonochemical synthesis of silver vanadium oxide micro/nanorods: Solvent and surfactant effects. Ultrason Sonochem 2013;20: 354–65. https://doi.org/10.1016/j.ultsonch.2012.05.002.

[25] Amiri M, Pardakhti A, Ahmadi-Zeidabadi M, Akbari A, Salavati-Niasari M. Magnetic nickel ferrite nanoparticles: Green synthesis by Urtica and therapeutic effect of frequency magnetic field on creating cytotoxic response in neural cell lines. Colloids Surf B Biointerfaces 2018;172:244–53. https://doi.org/10.1016/j.colsurfb.2018.08.049.

[26] Koçer Kızılduman B. Effect of fullerene (C_{70}) on the structural, morphological, optical and thermal properties of poly(butyl methacrylate) (PBMA). Fuller Nanotub Carbon Nanostruct 2024;33:275–87. https://doi.org/10.1080/1536383X.2024.2416996.

[27] Anasori B, Lukatskaya M, Gogotsi Y. 2D metal carbides and nitrides (MXenes) for energy storage. Nat Rev Mater 2017;2:16098. https://doi.org/10.1038/natrevmats.2016.98.

[28] Schlapbach L, Züttel A. Hydrogen-storage materials for mobile applications. Nature 2001;414:353–8. https://doi.org/10.1038/35104634.

[29] Doğan M, Sabaz P, Bïcïl Z, Kizilduman BK, Turhan Y. Activated carbon synthesis from tangerine peel and its use in hydrogen storage. J Energy Inst 2020;93: 2176–85. https://doi.org/10.1016/j.joei.2020.05.011.

[30] Çakır Ü, Kestel F, Kızılduman BK, Bicil Z, Doğan M. Multi-walled carbon nanotubes functionalized by hydroxyl and Schiff base and their hydrogen storage properties. Diam Relat Mater 2021;120:108604. https://doi.org/10.1016/j.diamond.2021.108604.

[31] Isinkaralar K, Gullu G, Turkyilmaz A, Dogan M, Turhan O. Activated carbon production from horse chestnut shells for hydrogen storage. Int J Glob Warm 2022; 26:361–73. https://doi.org/10.1504/IJGW.2022.122430.

[32] Pupysheva OV, Farajian AA, Yakobson BI. Fullerene nanocage capacity for hydrogen storage. Nano Lett 2008;8:767–74. https://doi.org/10.1021/nl071436g.

[33] Musyoka NM, Ren J, Langmi HW, North BC, Mathe M, Bessarabov D. Synthesis of rGO/Zr-MOF composite for hydrogen storage application. J Alloys Compd 2017; 724:450–5. https://doi.org/10.1016/j.jallcom.2017.07.040.

[34] Iijima S. Helical microtubules of graphitic carbon. Nature 1991;354:56–8. https://doi.org/10.1038/354056a0.

[35] Tahermansouri H, Aryanfar Y, Biazar E. Synthesis, characterization, and the influence of functionalized multi-walled carbon nanotubes with creatinine and 2-aminobenzophenone on the gastric cancer cells. Bull Korean Chem Soc 2013;34: 149–53. https://doi.org/10.5012/bkcs.2013.34.1.149.

[36] Azizian J, Chobfrosh Khoei D, Tahermansouri H, Yadollahzadeh K. Functionalization of carboxylated multi-walled carbon nanotubes with 1,4-phenylendiamine, phenylisocyanate and phenylisothiocyanate. Fuller Nanotub Carbon Nanostruct 2011;19:753–60. https://doi.org/10.1080/1536383X.2010.515762.

[37] Çalışır Ü, Çiçek B, Doğan M. Microwave-assisted cross-coupling synthesis of aryl functionalized MWCNTs and investigation of hydrogen storage properties. Fullerenes Nanotubes Carbon Nanostruct 2021;29:899–906. https://doi.org/10.1080/1536383X.2021.1913727.

[38] Yalçinkaya FN, Doğan M, Bicil Z, Kizilduman BK. Effect of functionalization and Li-doping methods to hydrogen storage capacities of MWCNTs. Fuel 2024;372: 132274. https://doi.org/10.1016/j.fuel.2024.132274.

[39] Çakır Ü, Doğan M, Kızılduman BK, Bicil Z. Functionalized and Schiff base based multi-walled carbon nanotubes for hydrogen storage. J Alloys Compd 2025;1010: 177290. https://doi.org/10.1016/j.jallcom.2024.177290.

[40] Doğan M, Turan M, Beyli PT, Bicil Z, Kızılduman BK. Thermal and kinetic properties of poly(vinylacetate)/modified MWCNT nanocomposites. Fullerenes Nanotubes Carbon Nanostruct 2021;29:475–85. https://doi.org/10.1080/1536383X.2020.1860945.

[41] Doğan M, Selek A, Turhan O, Kızılduman BK, Bicil Z. Different functional groups functionalized hexagonal boron nitride (h-BN) nanoparticles and multi-walled carbon nanotubes (MWCNT) for hydrogen storage. Fuel 2021;303:121335. https://doi.org/10.1016/j.fuel.2021.121335.

[42] Doğan EE. Hydrogen production and its storage from solar energy. Adv Mater Sci 2020;20:14–25. https://doi.org/10.2478/adms-2020-0007.

[43] Francisco W, Ferreira FV, Ferreira EV, Cividanes LDS, Coutinho ADR, Thim GP. Functionalization of multi-walled carbon nanotube and mechanical property of epoxy-based nanocomposite. J Aerosp Technol Manag 2015;7:289–93. https://doi.org/10.5028/jatm.v7i3.485.

[44] Ferreira FV, Francisco W, de Menezes BRC, Cividanes LDS, dos Reis Coutinho ADR, Thim GP. Carbon nanotube functionalized with dodecylamine for the effective dispersion in solvents. Appl Surf Sci 2015;357:2154–9. https://doi.org/10.1016/j.apsusc.2015.09.202.

[45] Cividanes LS, Simonetti EA, Moraes MB, Fernandes FW, Thim GP. Influence of carbon nanotubes on epoxy resin cure reaction using different techniques: a comprehensive review. Polym Eng Sci 2014;54:2461–9. https://doi.org/10.1002/pen.23775.

[46] Zhang A, Tang M, Luan J, Li J. Noncovalent functionalization of multi-walled carbon nanotubes with amphiphilic polymers containing pyrene pendants. Mater Lett 2012;67:283–5. https://doi.org/10.1016/j.matlet.2011.09.103.

[47] Behnam B, Shier WT, Nia AH, Abnous K, Ramezani M. Non-covalent functionalization of single-walled carbon nanotubes with modified polyethyleneimines for efficient gene delivery. Int J Pharm 2013;454:204–15. https://doi.org/10.1016/j.ijpharm.2013.06.057.

[48] Khan MU, Gomes VG, Altarawneh IS. Synthesizing polystyrene/carbon nanotube composites by emulsion polymerization with non-covalent and covalent functionalization. Carbon 2010;48:2925–33. https://doi.org/10.1016/j.carbon.2010.04.029.

[49] Moya A, Cherevan A, Marchesan S, Gebhardt P, Prato M, Eder D, et al. Oxygen vacancies and interfaces enhancing photocatalytic hydrogen production in mesoporous CNT/TiO2 hybrids. Appl Catal B Environ 2015;179:574–82. https://doi.org/10.1016/j.apcatb.2015.05.052.

[50] Tofighy MA, Mohammadi T. Nickel ions removal from water by two different morphologies of induced CNTs in mullite pore channels as adsorptive membrane. Ceram Int 2015;41:5464–72. https://doi.org/10.1016/j.ceramint.2014.12.116.

[51] Graupner R. Raman spectroscopy of covalently functionalized single-wall carbon nanotubes. J Raman Spectrosc 2007;38:673–83. https://doi.org/10.1002/jrs.1694.

[52] Müller M, Maultzsch J, Wunderlich D, Hirsch A, Thomsen C. Raman spectroscopy on chemically functionalized carbon nanotubes. Phys Status Solidi B 2007;244: 4056–9. https://doi.org/10.1002/pssb.200776119.

[53] Kumar AM, Gasem ZM. Effect of functionalization of carbon nanotubes on mechanical and electrochemical behavior of polyaniline nanocomposite coatings. Surf Coat Technol 2015;276:416–23. https://doi.org/10.1016/j.surfcoat.2015.06.036.

[54] Okutan E, Çoşut B, Kayıran SB, Durmuş M, Kılıç A, Yeşilot S. Synthesis of a dendrimeric phenoxy-substituted cyclotetraphosphazene and its non-covalent interactions with multiwalled carbon nanotubes. Polyhedron 2014;67:344–50. https://doi.org/10.1016/j.poly.2013.09.011.

[55] Avilés F, Ponce A, Cauich-Rodríguez JV, Martínez GT. TEM examination of MWCNTs oxidized by mild experimental conditions. Fullerenes Nanotubes Carbon Nanostruct 2012;20:49–55. https://doi.org/10.1080/1536383X.2010.533308.

[56] Cho JH, Park CR. Hydrogen storage on Li-doped single-walled carbon nanotubes: Computer simulation using the density functional theory. Catal Today 2007;120: 407–12. https://doi.org/10.1016/j.cattod.2006.09.027.

[57] Bicil Z, Doğan M. Characterization of activated carbons prepared from almond shells and their hydrogen storage properties. Energy Fuels 2021;35:10227–40. https://doi.org/10.1021/acs.energyfuels.1c00795.

[58] Ferreira FV, Cividanes LDS, Brito FS, Menezes BRCD, Franceschi W, Nunes Simonetti EA, et al. Functionalization of carbon nanotube and applications. In: Functionalizing graphene and carbon nanotubes: a review. Springer; 2016. p. 31–61.

[59] Doğan M, Alkan M, Türkyilmaz A, Özdemir Y. Kinetics and mechanism of removal of methylene blue by adsorption onto perlite. J Hazard Mater 2004;109:141–8. https://doi.org/10.1016/j.jhazmat.2004.03.003.

[60] Jhung SH, Kim HK, Yoon JW, Chang JS. Low-temperature adsorption of hydrogen on nanoporous aluminophosphates: effect of pore size. J Phys Chem B 2006;110: 9371–4. https://doi.org/10.1021/jp061272c.

[61] Yang Z, Wang W, Dong M, Wang J, Li Y, Gong H, et al. A model of dynamic adsorption–diffusion for modeling gas transport and storage in shale. Fuel 2016; 173:115–28. https://doi.org/10.1016/j.fuel.2016.01.037.

[62] Tran HN. Is it possible to draw conclusions (adsorption is chemisorption) based on fitting between kinetic models (pseudo-second-order or Elovich) and experimental data of time-dependent adsorption in solid-liquid phases?, recent Innov. Chem Eng 2022;15:228–30. https://doi.org/10.2174/2405520416666221202085740.

[63] Revellame ED, Fortela DL, Sharp W, Hernandez R, Zappi ME. Adsorption kinetic modeling using pseudo-first order and pseudo-second order rate laws: a review. Cleaner Eng Technol 2020;1:100032. https://doi.org/10.1016/j.clet.2020.100032.

[64] Doğan M, Abak H, Alkan M. Adsorption of methylene blue onto hazelnut shell: kinetics, mechanism and activation parameters. J Hazard Mater 2009;164:172–81. https://doi.org/10.1016/j.jhazmat.2008.07.155.
[65] Doğan M, Alkan M, Demirbaş Ö, Özdemir Y, Özmetin C. Adsorption kinetics of maxilon blue GRL onto sepiolite from aqueous solutions. Chem Eng J 2006;124:89–101. https://doi.org/10.1016/j.cej.2006.08.016.
[66] Doğan M, Kalafat MY, Kizilduman BK, Bicil Z, Turhan Y, Yanmaz E, et al. Hydrogen storage analysis of fullerene and defective fullerenes: the first experimental study. Fuel 2025;390:134705. https://doi.org/10.1016/j.fuel.2025.134705.
[67] Doğan M, Turhan Y, Kızılduman BK, Turan Beyli P, Doğan S. Isothermal calcination kinetics of boric acid and its use for nano boron oxide production under cryogenic conditions. Inorg Nano-Met Chem 2024:1–10. https://doi.org/10.1080/24701556.2024.2356039.
[68] Matsumoto I, Asano K, Sakaki K, Nakamura Y. Hydrogen absorption kinetics of magnesium fiber prepared by vapor deposition. Int J Hydrogen Energy 2011;36:14488–95. https://doi.org/10.1016/j.ijhydene.2011.08.029.
[69] Ho YS. Removal of copper ions from aqueous solution by tree fern. Water Res 2003;37:2323–30. https://doi.org/10.1016/S0043-1354(03)00002-2.
[70] Weber Jr WJ, Morris JC. Kinetics of adsorption on carbon from solution. J Sanit Eng Div 1963;89:31–59. https://doi.org/10.1061/JSEDAI.0000430.
[71] Alkan M, Doğan M, Turhan Y, Demirbaş Ö, Turan P. Adsorption kinetics and mechanism of maxilon blue 5G dye on sepiolite from aqueous solutions. Chem Eng J 2008;139:213–23. https://doi.org/10.1016/j.cej.2007.07.080.
[72] Turkyilmaz A, Isinkaralar K, Dogan M, Kizilduman BK, Bicil Z. Production, characterization, and hydrogen storage properties of activated carbon from horse chestnut shell. Sustain Chem Pharm 2024;40:101634. https://doi.org/10.1016/j.scp.2024.101634.
[73] Sales DC, Martins RG, Jaguaribe EF, Abreu CA. Effect of the intra-particle diffusion and porous structure on models for adsorption and storage of methane onto activated carbons. Adsorpt Sci Technol 2012;30:729–37. https://doi.org/10.1260/0263-6174.30.8-9.729.
[74] Kızılduman BK, Turhan Y, Doğan M. Mesoporous carbon spheres produced by hydrothermal carbonization from rice husk: Optimization, characterization and hydrogen storage. Adv Powder Technol 2021;32:4222–34. https://doi.org/10.1016/j.apt.2021.09.025.